Co-Sn Nanocrystalline Solid Solutions as Anode Material in Lithium-Ion Batteries with high pseudocapacitive contribution

Junshan Li,[a,b,○] Xijun Xu,[c,d,○] Jun Liu,[c,d,*] Zhishan Luo,[a] Chaoqi Zhang,[a] Ting Zhang,[e] Pengyi Tang,[e] Maria Francisca Infante Carrió,[e] Jordi Arbiol,[e,f] Jordi Llorca,[g] Andreu Cabot[a,f,*]

a Catalonia Institute for Energy Research - IREC, Sant Adrià de Besòs, Barcelona, 08930, Spain

b Departament d'Electronica, Universitat de Barcelona, 08028 Barcelona, Spain

c Guangdong Provincial Key Laboratory of Advanced Energy Storage Materials, School of Materials Science and Engineering, South China University of Technology, Guangzhou 510641, P. R. China

d SUNWODA-SCUT Joint Laboratory for Advanced Energy Storage Technology, South China University of Technology, Guangzhou 510641, P. R. China

e Catalan Institute of Nanoscience and Nanotechnology (ICN2), CSIC and BIST, Campus UAB, Bellaterra, 08193 Barcelona, Spain

f ICREA, Pg. Lluís Companys 23, 08010 Barcelona, Spain

g Institute of Energy Technologies, Department of Chemical Engineering and Barcelona Research Center in Multiscale Science and Engineering. Universitat Politècnica de Catalunya, EEBE, 08019 Barcelona, Spain

Abstract: Co-Sn solid-solution nanoparticles with the Sn crystal structure and tuned metal ratios were synthesized by a facile one-pot solution-based procedure involving the initial reduction of a Sn precursor and the posterior incorporation of Co within the Sn lattice. Such nanoparticles were used as anode materials for Li-ion batteries. Among the different compositions tested, $Co_{0.9}Sn$ electrodes provided the best performance, with a stable average capacity of over 600 mAh g^{-1} and 400 mAh g^{-1} at current densities of 0.2 A g^{-1} and 1.0 A g^{-1}, respectively. Up to 81 % pseudocapacitance contribution at a sweep rate of 1.0 mV s^{-1} were measured for this electrode, ensuring fast kinetics and long durability. The excellent performance of Co-Sn alloy NP-based electrodes was associated to both the small size of the crystal domains and the proper composition.

Keywords: Colloidal; Bimetallic; Nanoparticles; Tin; Tin Cobalt; Alloy; Pseudocapacitance; Anode; Lithium-ion Batteries

INTRODUCTION

While lithium-ion batteries (LIBs) have become the dominant energy storage technology in numerous fields, their limited energy density, charging rate, and stability are still critical performance parameters to be improved.[1–4] This improvement requires optimization of both anode and cathode materials. At the anode, current commercial LIBs use graphite, which has a relatively low maximum theoretical capacity (372 mAh g^{-1} to form LiC_6).[5] Alternative anode materials such as Sn, Ge and Si provide platforms with higher lithium storage capacities: $Li_{22}Sn_5$ (994 mAh g^{-1}), $Li_{22}Ge_5$ (1600 mAh g^{-1}), and $Li_{22}Si_5$ (3000 mAh g^{-1}) respectively.[6–8] Among these candidates material, Sn and Sn-based compounds are particularly appealing owing to their abundance, low cost and high electrical conductivity. [1,7,9,10]

In terms of stability, the huge lattice expansion and contraction during cycling strongly reduces the battery performance due to a loss of electrical connection by electrode pulverization. In the case of Sn, a 300% volume change is associated to the $Sn/Li_{22}Sn_5$ reaction. Different strategies have been defined to tackle down this issue. One main approach is to alloy the active phase with a second elements that buffers the volume changes.[4,7,9,11] In this direction, Sn-based alloys with Ni,[9,12–14] Co,[11,15–29] Fe,[13,23] Cu,[13,30] and Sb[31,32]) have demonstrated superior cycling performance than bare Sn anodes. Among the different Sn-based alloys tested, CoSn electrodes have shown particularly promising performances as anode materials for LIBs and Co-Sn-C composites have been even used in commercial batteries, what has motivated a notable interest in this system.[7,19,33] Most previous works have focused on intermetallic Co-Sn alloys: Co_3Sn_2, CoSn, $CoSn_2$. While some controversy remains, most works has considered $CoSn_2$ as the optimum composition among the different possible Co-Sn intermetallics, due to its highest content of Sn, the electroactive element. However, beyond intermetallics, a range of Co-Sn solid solutions exist that are yet to be explored.

Besides alloying the active material to improve cycling peformance, the use of nanostructured electrodes can reduce the accumulated stress during lithiation, even at high rates, thus diminishing mechanical disintegration and improving stability. Furthermore, nanosized materials present additional advantages, such as a fast rate capability because of the shorter Li-ion diffusion paths and a potentially high pseudocapacitive contribution associated with their high surface/volume ratio.[34] This pseudocapactivive contribution is particularly appealing as it can significantly improve both the rate performance of LIBs and at the same time their stability.

In the present work, we take advantage of the versatility of colloidal synthesis method to produce nanoparticles (NPs) with controlled crystal phase and composition, to produce Co-Sn solid solution NPs with tuned Co:Sn ratios, from 0.3 to 1.3. After removing surface ligands, we use these NPs to test the performance capacitive behavior and stability of Co-Sn solid solutions as anode material for LIBs, demonstrating this system to be characterized by a high pseudocapacitive contribution.

EXPERIMENTAL

Colloidal synthesis of Sn and Co-Sn NPs: Syntheses were carried out using standard air-free techniques. All the reagents and solvent were analytical grade and used without further purification. In a typical synthesis of Co-Sn NPs with nominal composition Co:Sn = 3:2, 0.6 mmol cobalt(II) acetylacetonate ($Co(acac)_2$, 99%, Sigma-Aldrich) and 0.4 mmol tin(II) acetate ($Sn(OAc)_2$, 95%, Fluka) were added into a 50 mL three-neck round-bottomed flask. Subsequently, 20 mL of oleylamine (OAm, 80-90%, TCI) and 1.0 mL of oleic acid (OAc, Sigma-Aldrich) were loaded along with a magnetic bar in a three-neck flask connected with a thermometer, condenser and septum. The flask was heated to 80 °C and degassed under vacuum for 2 hours and then backfilled with Ar. Then, 5 mL of tri-n-octylphosphine (TOP, 97%, Strem) were injected, and afterward the solution was heated up to 180 ºC at 5 °C min^{-1}. Right after reaching 180 °C, 5 mL of a degassed OAm solution containing 5 mmol of borane tert-butylamine (TBAB, 97%, Sigma-Aldrich) was injected. Upon injection of this reducing complex, the solution became black, but the reaction mixture was maintained at 180 ºC for 1 hour to allow the NPs to grow. After 1h, the heating mantle was removed and the solution was cooled down to room temperature in approximately 3 min using a water bath. NPs were collected by centrifugation (approximately 3 min) after adding an excess of acetone. The precipitate was dispersed in chloroform and centrifuged a second time with an excess of acetone. This washing process was repeated for three times. Finally, NPs were stored in chloroform.

Ligand removal: 25 mL of acetonitrile containing 0.8 mL hydrazine hydrated were added into a vial containing about 100 mg of precipitated NPs. The solution was strongly stirred for 4 hours and centrifuged. The NPs were further washed with acetonitrile 3 more times, followed by vacuum-drying at room temperature. The product was kept in an Ar-filled glove box.

Characterization: X-ray diffraction (XRD) patterns were recorded at room temperature on a Bruker AXS D8 Advance X-ray diffractometer with Cu K radiation (λ = 1.5106 Å) operating at 40 kV and 40 mA. Transmission electron microscopy (TEM) analyses were performed on a ZEISS LIBRA 120, operating at 120 kV. High-resolution TEM (HRTEM) and scanning TEM (STEM) studies were carried out using a field emission gun FEI Tecnai F20 microscope at 200 kV with a point-to-point resolution of 0.19 nm. High angle annular dark-field (HAADF) STEM was combined with electron energy loss spectroscopy (EELS) in the Tecnai microscope by using a GATAN QUANTUM filter. Composition analysis was carried out using a ZEISS Auriga Scanning electron microscopy (SEM) equipped with an energy dispersive X-ray spectroscopy (EDS) detector operated at 20 kV. X-ray photoelectron spectroscopy (XPS) measurements were carried out in normal emission using an Al anode XR50 source operating at 150 mW and a Phoibos 150 MCD-9 detector. Fourier transform infrared spectrometer (FTIR) data was recorded on an Alpha Bruker spectrometer.

Electrochemical measurements: To evaluate the intrinsic electrochemical performance of Co-Sn NPs, the working electrode was prepared by mixing dried NPs, Super P and polyvinylidene fluoride (PVDF) with a weight ratio of 80:10:10 in an appropriate amount of N-methy1-2-pyrrolidone (NMP) to obtain a slurry, then

the mixture was coated onto a Cu foil. Then, it was dried in a vacuum oven at 80 ºC for 24 h. Subsequently, the foil was cut into disks with a diameter of 12 mm. The typical mass loading of active materials was estimated to be 0.7-1.2 mg cm^{-2}. To test the performance of electrodes based on Co-Sn NPs, half cells were assembled in the glove box (H_2O and O_2 < 0.1 ppm) using Celgard2400 as separator. As electrolyte, a 1 M $LiPF_6$ solution in ethylene carbonate (EC)/diethyl carbonate (DEC) (1:1 in volume) with 5 wt% fluoroethylene carbonate (FEC) as additive was used. Galvanostatic charge-discharge were measured by a battery test system (CT2001A, LAND) with cutoff potentials from 0.01 V to 3.0 V. Cyclic voltammetry (CV) curves were performed by an electrochemical workstation (Gamry Interface 1000) in the voltage range from 0–3.0 V and the scan rate from 0.1 mV s^{-1} to 1 mV s^{-1}.

RESULTS AND DISCUSSION

Colloidal Co-Sn NPs were produced by the reduction of tin and cobalt precursors with TBAB at 180 °C in a solution containing OAm, OAc and TOP (see details in experimental section, Figure 1a). Figures 1b-c show representative TEM micrographs and size distribution histograms of the quasi-spherical NPs produced. The average NP size was estimated to be in the range from 6 nm to 10 nm, depending on the compositions. XRD analysis showed all the NPs to conserve the Sn crystal structure, although XRD patterns appeared shifted to lower angles, as it corresponds to the introduction of a slightly larger atom, Co, within the Sn structure. The similar XRD patterns obtained for all the different compositions was somehow surprising taking into account previous reports showing the formation of intermetallics, i.e. $CoSn_2$, CoSn and Co_3Sn_2, when co-reducing proper amounts of the two elements.

EDX analysis showed the Co:Sn ratio in Co-Sn solid-solution NPs to be: 1.3, 0.9, 0.7 and 0.3 when produced from nominal Co:Sn precursor ratios of 2:1, 3:2, 1:1 and 1:2, respectively. The final NP stoichiometry and the pink color of the supernatant obtained after NP precipitation revealed that some of the cobalt precursor remained unreacted after 1h at 180 ºC. We also observed that the same reaction conditions but in the absence of Sn precursor did not result in the formation of Co NPs. On the contrary, the same reaction in the absence of Co, resulted in the formation of Sn NPs. We believe that in the reaction conditions used, the Sn precursor was first reduced to nucleate Sn NPs. To these initial Sn NPs, some of the Co ions within the solution were being incorporated upon reduction with TBAB, during the 1h period at 180 ºC. Through this synthesis mechanism, the Sn crystal structure was conserved, which is in contrast to the results obtained in previous works that make use of higher reaction, alloying or annealing temperatures to produce Co-Sn alloys.

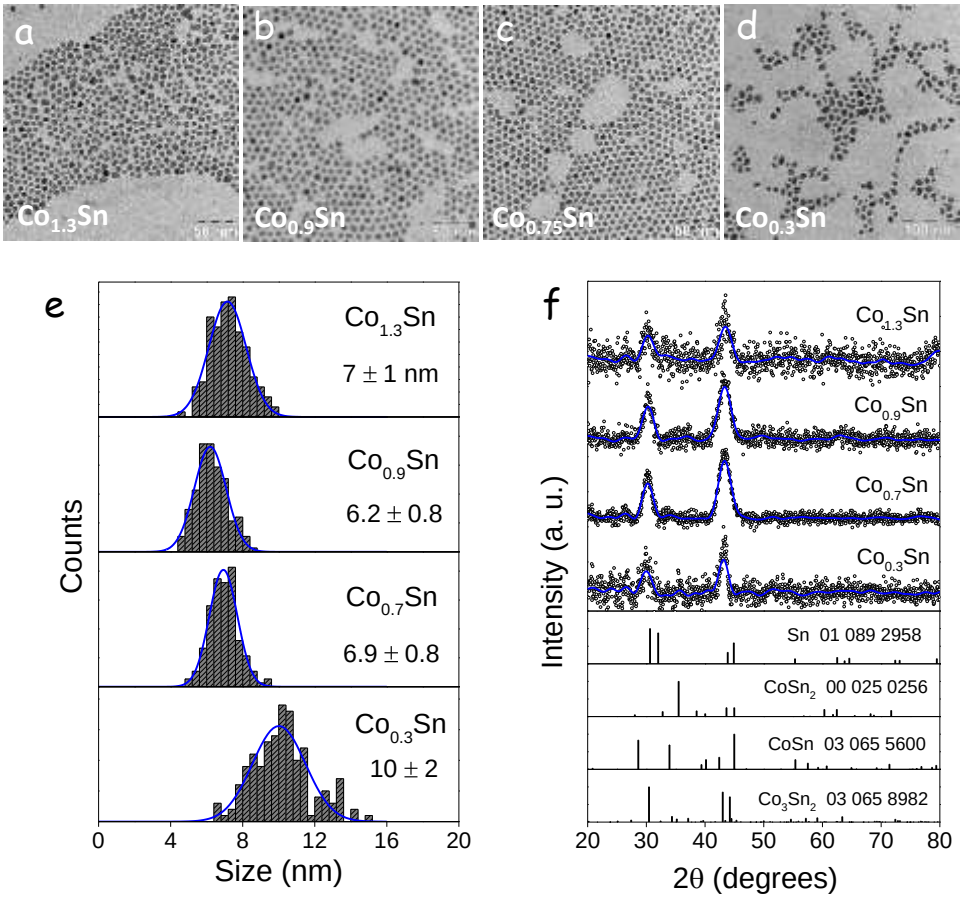

Figure 1. a-d) TEM micrographs of Co-Sn NPs with different compositions, as displayed in each image. e) Size distribution histograms of the Co-Sn NPs; f) XRD patterns of the NPs with different compositions. Sn and different Co-Sn intermetallic XRD patterns are shown as reference.

XPS analysis (Figure S2) showed the Co:Sn ratio of the $Co_{0.9}Sn$ NPs to be 0.7, which pointed at a slightly Sn-rich surface. This Sn-rich surface may be related to a slight oxidation of the NPs exposed to ambient conditions. Air exposure could result in a slight restructuration of the alloy due to the higher Sn affinity to oxygen which drove the diffusion of Sn to the surface.

Figure 2a shows STEM micrographs and EELS chemical composition maps of the $Co_{0.9}Sn$ NPs. All NPs contained the two elements in similar ratios. Within each NP, while Co and Sn distributions were mostly homogeneous, most NPs present a Sn-rich shell. HRTEM micrographs (Figure 2b) more clearly displayed the core-shell structure of the NPs. From HRTEM analysis, the core crystal structure could be assigned to the $Co_{2.9}Sn_2$ orthorhombic phase (space group = Pnma) with a = 7.1450 Å, b = 5.2500 Å and c = 8.1730 Å, or to the Co_3Sn_2 hexagonal phase (space group = P63/mmc) with a = b = 4.1130 Å and c = 5.1850 Å (SI). This result is in contradiction with XRD data and the compositional and XPS analysis. We hypothesize that solid-solution NPs with the $Co_{0.9}Sn$ composition and Sn structure were initially formed. With the exposition to air, these NPs developed a Sn-rich surface associated to a differential reactivity of the two elements with oxygen.

Within the electron beam, the core, having a higher Co content due to the diffusion of Sn to the surface, crystallized to an intermetallic Co_3Sn_2 phase with potential additional Sn segregation to the surface.

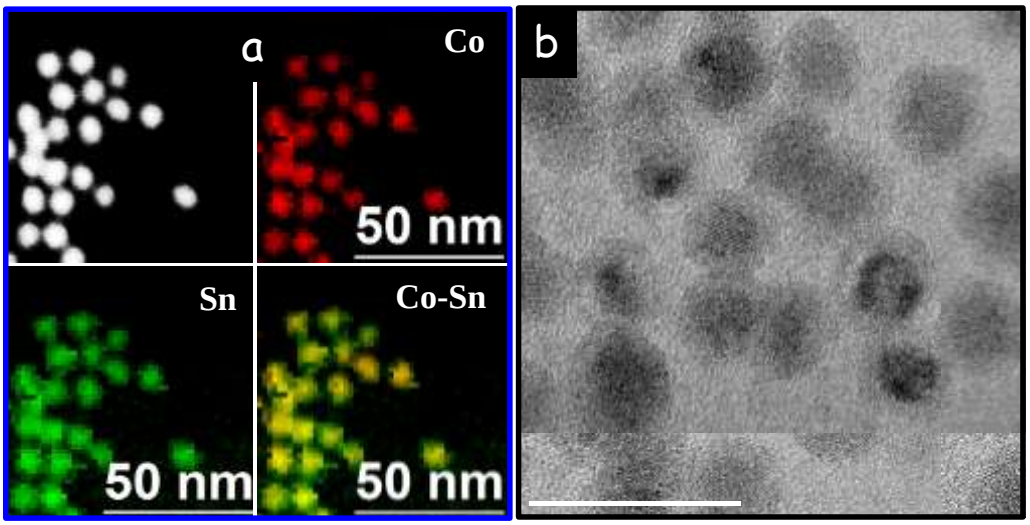

Figure 2. a) STEM and EELS compositional maps of $Co_{0.9}Sn$ NPs. b) HRTEM micrograph of $Co_{0.9}Sn$ NPs exposed to atmosphere and displaying a core-shell type structure.

Co-Sn NPs were explored as anode material in LIBs. Before testing their performance, the organic ligands used to control the growth of the NPs in solution were removed by treating them with a mixture of hydrazine and acetonitrile (Figure S4).[31,35] Anodes were prepared by casting an non-aqueous slurry containing 80 wt% of active material, polyvinylidene (PVDF, 10 wt%) as a polymer binder, and Super P as conductive additive (10 wt%). After vacuum drying, all anodes had similar mass loading of the active materials (ca. 0.79-1.36 mg). All electrodes were tested under the same conditions, using coin type half-cells with metallic Li as counter electrodes.

The electrochemical performance of Co-Sn NPs was initially assessed through cyclic voltammetry (CV) with a scan rate of 0.1 mV s^{-1} in the potential window of 0-3.0 V (vs. Li^+/Li). As shown in Figures 3, all CV cycles showed a similar trend, but the initial two cycles displayed more pronounced peaks than following ones at 1.31 V in the forward scan and 0.65 V and 1.45 V in the reverse one. Differences were ascribed to the formation of the solid electrolyte interphase (SEI) layer during the first cycles, in agreement with previous works using an electrode of similar composition.[36] The overlap of the 3rd and subsequent cycles indicated good stability of the electrode. The three cathodic peaks at 1.45, 0.65, 0.05 V were associated to the reversible lithium insertion in the CoSn alloy to form $Li_{4.4}Sn$. During the anodic sweep, peaks at 0.52, 1.31, 2.05 V were related to the extraction of Li ions from the electrode. Qualitatively similar voltammograms were obtained for the four compositions tested.

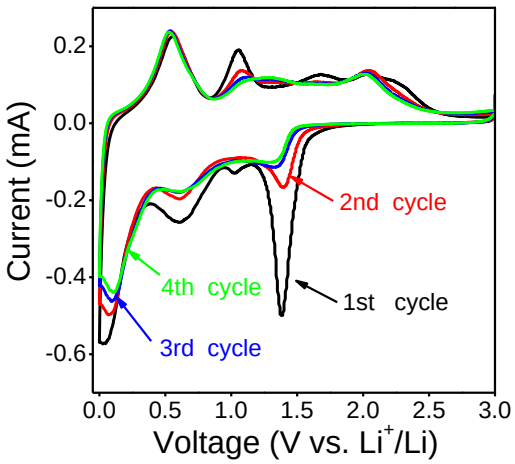

Figure 3. Initial cyclic voltammograms obtained from the $Co_{0.9}Sn$ electrode in the voltage window 0-3.0 V vs. Li^+/Li at 0.1 mV s^{-1}.

Figures 4a-d display the first three charge-discharge cycles at a current density of 0.2 A g^{-1} of the electrodes containing Co-Sn NPs with different compositions. For all the compositions tested, small charging and discharging plateaus were observed at around 0.5 V and 1.6 V, respectively. Figure 4e-f shows the charge-discharge capacity and related efficiency over 400 cycles at a current density of 1.0 A g^{-1} (activated at 0.2 and 0.5 A g^{-1} for 10 cycles respectively). All compositions showed a similar trend, with an initial decrease of the capacity, attributed to the SEI formation, which after a certain number of cycles was recovered. At much larger cycle numbers, a moderate and sustained decrease of capacity was observed. An initial increase of coulombic efficiency, from ca. 50 % to ca 98 % was simultaneously obtained for all the electrodes tested. This coulombic efficiency was stabilized after the first few cycles.

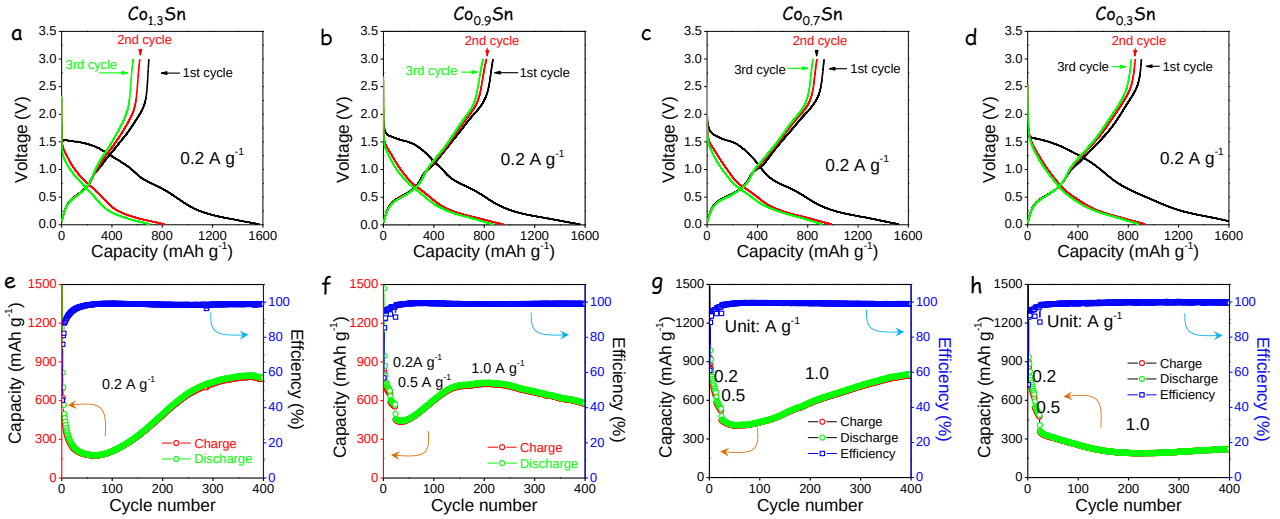

Figure 4. a-d) Initial charge-discharge curves at 0.2 A g^{-1} for the different electrode compositions as displayed on the top of each graph. e-h) Charge-discharge capacity and related efficiency over 400 cycles at a current density of 1.0 A g^{-1}: activated at 0.2 and 0.5 A g^{-1} for 10 cycles each. For the $Co_{1.3}Sn$ electrode only data at 0.2 A g^{-1} is shown.

$Co_{0.9}Sn$ and $Co_{0.7}Sn$ electrodes showed the highest Li storage capacities among the compositions tested. For the $Co_{0.9}Sn$ electrode at 0.2 A g^{-1}, as shown in Figure S5, during the first cycle, the coulombic efficiency was

just 55.7%, with a high discharge (869 mAh g^{-1}) and charge capacity (1560 mAh g^{-1}). A strong capacity loss was observed during the first cycles, down to charge and discharge capacities of 629 mAh g^{-1} and 647 mAh g^{-1} with 97.2% coulombic efficiency at the 24th cycle. With continuous cycling, the coulombic efficiency remained stable and the capacity gradually increased up to charge and discharge capacities of 1534 mAh g^{-1} and 1555 mAh g^{-1} at the 220th cycle. Figure S6 compares the EIS results in selected charge-discharge process in the first and the 400th cycle (1 A g^{-1}). Both of them have small charge-transfer resistances.

To evaluate the rate capability of the Co-Sn electrodes, galvanostatic cycling was performed at current rate between 0.05 to 4 A g^{-1} (Figure 5a). Figure 5b presents the corresponding charge-discharge profiles from 0.05 to 4.0 A g^{-1}. For $Co_{0.9}Sn$, the electrode delivered a discharge capacity of 804, 702, 598, 532, 448, 365, 267 mAh g^{-1} at 0.05, 0.1, 0.2, 0.5, 1.0, 2.0, 4.0 A g^{-1}, respectively.

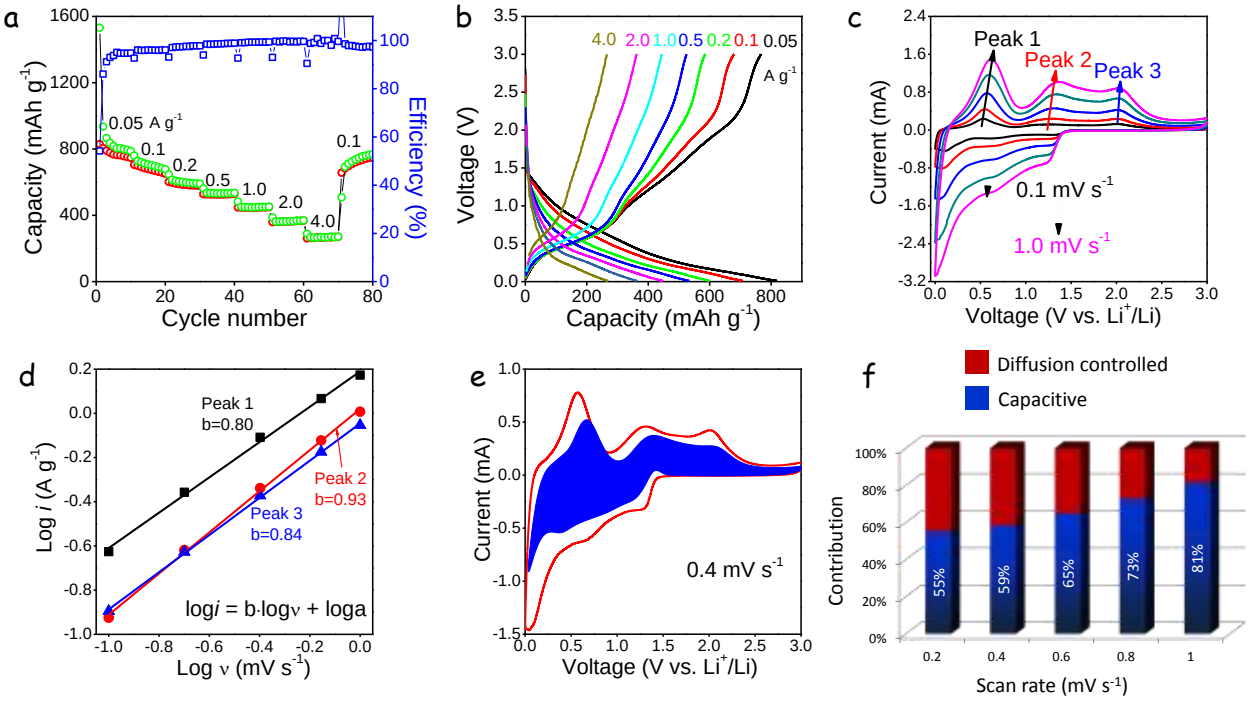

Figure 5. Li-ion storage performance of the $Co_{0.9}Sn$ electrode: a) Charge-discharge curves at rates: 0.05, 0.1, 0.2, 0.5, 1.0, 2.0, 4.0, 0.1 A g^{-1}. b) Rate performance at 0.05, 0.1, 0.2, 0.5, 1.0, 2.0, 4.0 A g^{-1}. c) CV curve at the scan rates of 0.1, 0.2, 0.4, 0.7, 1.0 mV s^{-1}. d) Logarithmic dependence between peak current density and scan rate at the anodic peaks 0.52, 1.31, 2.05 V. e) Capacitive contribution to the total current contribution at 0.4 mV s^{-1}. f) Normalize capacitive and diffusion-controlled contribution at the scan rates of 0.1, 0.2, 0.4, 0.7, 1.0 mV s^{-1}.

The kinetics of the Co-Sn electrodes was further investigated using CV at different scan rates, from 0.1 to 1 mV s^{-1}. Figure 5c presents the CV curves obtained from the $Co_{0.9}Sn$ electrode at the scan rates of 0.1, 0.2, 0.4,

0.7, 1.0 mV s^{-1} in the potential range 0-3.0 V vs Li^+/Li. Three anodic peak were observed at 0.52, 1.31, 2.05 V, all of them increasing with the scan rate.

Two main charge-storage mechanisms determine the electrode storage capacity: i) a diffusion-controlled contribution associated to the $Li_{22}Sn_5$ alloy formation; and ii) a surface-related capacitive contribution known as the pseudocapacitive contribution.[37,38] The pseudocapacitive contribution is particularly attractive because it is a much faster and stable process, whereas the diffusion-controlled alloying is slower and generally provides relatively poor cycle life.

Generally, the relationship between the measured current (i) and the scan rate (v) can be expressed as:

$$i = av^b$$

According to previous report, a diffusion controlled process is characterized by a scan rate dependence with b = 0.5, whereas an ideal capacitive behavior translates into b = 1.[39–41] From the liner fit of the logarithmic plot of the current vs. scan rate (Figure 5d), b values of 0.80, 0.93 and 0.84 were calculated at 0.52, 1.31, 2.05 V, respectively. These values indicated a fast kinetics resulting from a pseudocapacitive effect.

At each potential, the current density contribution at a given scan rate could be divided into two parts, a diffusion-controlled ($k_1v^{1/2}$) and a capacitor-like fraction (k_2v):

$$i(V) = k_1v^{1/2} + k_2v$$

To distinguish the fraction of the current arising from Li^+ insertion and that from a capacitive process at each specific potential, k_1 and k_2 were determined by plotting $i(V)/v^{1/2}$ vs. $v^{1/2}$.[39,41] Figure 5e shows the CV profiles at 0.4 mV s^{-1} and compares the capacitive current (blue shaded region) with that for the total measured current (red curve) for the $Co_{0.9}Sn$ electrode. The relative pseudocapacitive contributions at sweep rates of 0.1, 0.2, 0.4, 0.7 and 1.0 mV s^{-1} were 55%, 59%, 65%, 73% and 81%, respectively (Figures 4f and S7). These results clearly suggest that the pseudocapacitive charge-storage amount does occupy a high portion of the whole energy storage capacity, which is associated to the small size of the Co-Sn NPs used and their Sn-rich and oxidized surface.

CONCLUSION

In conclusion, Co-Sn solid-solution NPs with average size in the 6-10 nm range were synthesized via simple one pot colloidal synthesis procedure. The NP composition was adjusted, CoxSn $1.3 \leq x \leq 0.3$, by tuning the ratio of the initial precursors. The low synthesis temperature favored the nucleation of Sn NPs and the subsequent inclusion of Co to the Sn lattice, forming a solid solution with virtually any composition, instead of an intermetallic compound. Co-Sn NPs presented a Sn rich surface after exposure to air. These Co-Sn solid solutions were tested as anode materials in LIBs on a half-cell battery system. Among the different

compositions tested, $Co_{0.9}Sn$ NPS provided the best performance, with a charge-discharge capacity above 600 mAh g^{-1} at 0.2 A g^{-1} over 220 cycles. At a higher current density, 1 A g^{-1}, a charge-discharge current density over 400 cycles of 437 mA g^{-1} was measured, which was much larger than that of graphite currently used in commercial devices. Through the kinetic analysis of $Co_{0.9}Sn$ NPS by the CV measurement, we found a very large pseucapacitive contribution, up to 81% at a sweep rate of 1 mV s^{-1}, which is related to the small size of the particles and probably to their SnOx-rich surface.

Author Information

○ J. Li and X. Xu equally contributed to this work.

Corresponding Author

* Andreu Cabot: acabot@irec.cat

* Jun Liu: msjliu@scut.edu.cn

Acknowledgments

J. Li thanks the China Scholarship Council for scholarship support. JA and TZ acknowledge funding from Generalitat de Catalunya 2014 SGR 1638 and the Spanish MINECO coordinated projects between IREC and ICN2 VALPEC and subprojects RESOL and ANAPHASE (ENE2017-85087-C3). ICN2 acknowledges support from the Severo Ochoa Programme (MINECO, Grant no. SEV-2013-0295) and is funded by the CERCA Programme / Generalitat de Catalunya. JL is a Serra Húnter Fellow and is grateful to ICREA Academia program and to MINECO/FEDER grant ENE2015-63969-R.

Conflict of interest

The authors declare no competing financial interest.

REFERENCES

1 C.-M. Park, J.-H. Kim, H. Kim and H.-J. Sohn, *Chem. Soc. Rev.*, 2010, **39**, 3115.

2 M. N. Obrovac and V. L. Chevrier, *Chem. Rev.*, 2014, **114**, 11444–11502.

3 R. Marom, S. F. Amalraj, N. Leifer, D. Jacob and D. Aurbach, *J. Mater. Chem.*, 2011, **21**, 9938.

4 P. G. Bruce, B. Scrosati and J.-M. Tarascon, *Angew. Chemie Int. Ed.*, 2008, **47**, 2930–2946.

5 L.-X. Ding, G.-R. Li, Z.-L. Wang, Z.-Q. Liu, H. Liu and Y.-X. Tong, *Chem. - A Eur. J.*, 2012, **18**, 8386–8391.

6 H. Tian, F. Xin, X. Wang, W. He and W. Han, *J. Mater.*, 2015, **1**, 153–169.

7 B. Wang, B. Luo, X. Li and L. Zhi, *Mater. Today*, 2012, **15**, 544–552.

8 C. K. Chan, R. N. Patel, M. J. O'Connell, B. A. Korgel and Y. Cui, *ACS Nano*, 2010, **4**, 1443–1450.

9 H. Ying and W.-Q. Han, *Adv. Sci.*, 2017, **4**, 1700298.

10 H. Ying and W.-Q. Han, 2017, **4**, 1700298.

11 S. Wang, M. He, M. Walter, F. Krumeich, K. V. Kravchyk and M. V. Kovalenko, *Nanoscale*, 2018, **10**, 6827–6831.

12 J. Liu, Y. Wen, P. A. van Aken, J. Maier and Y. Yu, *Nano Lett.*, 2014, **14**, 6387–6392.

13 X.-L. Wang, W.-Q. Han, J. Chen and J. Graetz, *ACS Appl. Mater. Interfaces*, 2010, **2**, 1548–1551.

14 M. Winter and J. O. Besenhard, *Electrochim. Acta*, 1999, **45**, 31–50.

15 N. Tamura, Y. Kato, A. Mikami, M. Kamino, S. Matsuta and S. Fujitani, *J. Electrochem. Soc.*, 2006, **153**, A1626.

16 R. Gnanamuthu, Y. N. Jo and C. W. Lee, *J. Alloys Compd.*, 2013, **564**, 95–99.

17 G. Ferrara, C. Arbizzani, L. Damen, M. Guidotti, M. Lazzari, F. G. Vergottini, R. Inguanta, S. Piazza, C. Sunseri and M. Mastragostino, *J. Power Sources*, 2012, **211**, 103–107.

18 J. He, H. Zhao, J. Wang, J. Wang and J. Chen, *J. Alloys Compd.*, 2010, **508**, 629–635.

19 S.-I. Lee, S. Yoon, C.-M. Park, J.-M. Lee, H. Kim, D. Im, S.-G. Doo and H.-J. Sohn, *Electrochim. Acta*, 2008, **54**, 364–369.

20 J. Zhang and Y. Xia, *J. Electrochem. Soc.*, 2006, **153**, A1466.

21 M. Walter, S. Doswald, F. Krumeich, M. He, R. Widmer, N. P. Stadie and M. V. Kovalenko, *Nanoscale*, 2018, **10**, 3777–3783.

22 Z. Du and S. Zhang, *J. Phys. Chem. C*, 2011, **115**, 23603–23609.

23 L. O. Vogt and C. Villevieille, *J. Mater. Chem. A*, 2017, **5**, 3865–3874.

24 J. Zhu, D. Wang, T. Liu and C. Guo, *Electrochim. Acta*, 2014, **125**, 347–353.

25 X. Shi, H. Song, A. Li, X. Chen, J. Zhou and Z. Ma, *J. Mater. Chem. A*, 2017, **5**, 5873–5879.

26 G. O. Park, J. Yoon, J. K. Shon, Y. S. Choi, J. G. Won, S. Bin Park, K. H. Kim, H. Kim, W.-S. Yoon and J. M. Kim, *Adv. Funct. Mater.*, 2016, **26**, 2800–2808.

27 B.-O. Jang, S.-H. Park and W.-J. Lee, *J. Alloys Compd.*, 2013, **574**, 325–330.

28 X. Liu, J. Xie, H. Zhao, P. Lv, K. Wang, Z. Feng and K. Świerczek, *Solid State Ionics*, 2015, **269**,

86–92.

29 J. R. González, F. Nacimiento, R. Alcántara, G. F. Ortiz and J. L. Tirado, *CrystEngComm*, 2013, **15**, 9196.

30 W. X. Lei, Y. Pan, Y. C. Zhou, W. Zhou, M. L. Peng and Z. S. Ma, *RSC Adv.*, 2014, **4**, 3233–3237.

31 M. He, M. Walter, K. V. Kravchyk, R. Erni, R. Widmer and M. V. Kovalenko, *Nanoscale*, 2015, **7**, 455–459.

32 M. He, K. Kravchyk, M. Walter and M. V. Kovalenko, *Nano Lett.*, 2014, **14**, 1255–1262.

33 F. Nacimiento, P. Lavela, J. L. Tirado and J. M. Jiménez-Mateos, *J. Solid State Electrochem.*, 2012, **16**, 953–962.

34 M. F. Oszajca, M. I. Bodnarchuk and M. V. Kovalenko, *Chem. Mater.*, 2014, **26**, 5422–5432.

35 J. Li, Z. Luo, Y. Zuo, J. Liu, T. Zhang, P. Tang, J. Arbiol, J. Llorca and A. Cabot, *Appl. Catal. B Environ.*, 2018, **234**, 10–18.

36 J. Shin, W.-H. Ryu, K.-S. Park and I.-D. Kim, *ACS Nano*, 2013, **7**, 7330–7341.

37 C. Chen, Y. Wen, X. Hu, X. Ji, M. Yan, L. Mai, P. Hu, B. Shan and Y. Huang, *Nat. Commun.*, 2015, **6**, 6929.

38 H.-S. Kim, J. B. Cook, S. H. Tolbert and B. Dunn, *J. Electrochem. Soc.*, 2015, **162**, A5083–A5090.

39 T.-C. Liu, W. G. Pell, B. E. Conway and S. L. Roberson, *J. Electrochem. Soc.*, 1998, **145**, 1882.

40 X. Xu, J. Liu, J. Liu, L. Ouyang, R. Hu, H. Wang, L. Yang and M. Zhu, *Adv. Funct. Mater.*, 2018, **28**, 1707573.

41 V. Augustyn, P. Simon and B. Dunn, *Energy Environ. Sci.*, 2014, **7**, 1597.